Automated Continuous Fields Prediction From Landsat Time Series: Application to Fractional Impervious Cover

Christopher R. Hakkenberg, Matthew P. Dannenberg, Conghe Song, and Giuseppe Vinci

***Abstract*— The characterization of fine temporal-resolution land surface dynamics from broadband optical satellite sensors is constrained by sparse acquisitions of high-quality imagery; interscene variation in radiometric, phenological, atmospheric, and illumination conditions; and subpixel variability in heterogeneous environments. In this letter, we address these concerns by developing and testing the automatic adaptive signature generalization and regression (AASGr) algorithm. Provided a robust reference map corresponding to the date of one image, AASGr automates the prediction of continuous fields maps from imagery time series that is adaptive to the spectral and radiometric characteristics of each target image and thereby requires neither atmospheric correction nor data normalization. We tested AASGr on a 22-year Landsat time series to quantify subannual impervious fractional cover dynamics in Houston, TX—an area characterized by a high degree of spatial heterogeneity in surface cover and high frequency in land cover change. The map time series achieved high accuracy in a three-part validation procedure and reveals spatio-temporal dynamics of urban intensification and extensification at a level of detail previously elusive in discrete classifications or coarse temporal-resolution map products. The automation of continuous fields time series is enabling a new generation of land surface products capable of characterizing precise morphologies along a continuum of spatio-temporal change. While AASGr was applied here to predict subpixel impervious fractional cover from Landsat imagery, the method is generalizable to a range of imagery and applications requiring dense continuous fields time series with uncertainty estimates of geophysical and biochemical characteristics, such as leaf area index, biomass, and albedo.**

***Index Terms*— Continuous fields, impervious cover, land cover change, landsat, machine learning, random forests (RFs), signature generalization, time series, urbanization.**

I. Introduction

THE steady deployment of satellite remote sensing platforms in recent decades has provided scientists with prodigious data streams of medium spatial resolution and broadband imagery for observing change on the earth surface [1]. Bitemporal change detection using image pairs has been used effectively to quantify state change (e.g., land cover class) or relative change in surface characteristics between two dates, but is unable to capture higher order temporal dynamics, including gradual change, periodicity, and change rates [2]. Reflecting the demand for more temporally frequent land surface data products for disparate applications from land cover change to biophysical land surface models [3], [4], the use of multitemporal image time series has increased rapidly [5].

Among all medium spatial resolution satellite sensors, the Landsat program stands out for providing consistent, multidecadal, high-quality land surface imagery [6]. However, even with Landsat sensor calibration and product quality assurance [7], the consistent characterization of multitemporal land surface dynamics is impeded by interscene and interimage variation in radiometric, phenological, atmospheric, and bidirectional reflectance distribution function (BRDF) and illumination conditions [8]. The general scarcity of high-quality, cloud-free image pairs at or near interannual anniversary dates only exacerbates the challenge of ensuring interdate consistency [9]. A number of approaches have been used to circumvent issues associated with sparsely acquired imagery, including input data enhancements like best-available-pixels composites, data blending, and multisensor data fusion techniques [10], [11] as well as compromises in model output such as the utilization of multiyear imagery for the characterization of a single, nominal year [12]. Despite this, interimage discrepancies may still require onerous and potentially confounding, data correction and normalization procedures that run the risk of exacerbating confusion between radiometric differences among image dates (noise) and land cover change (signal) [8].

Alongside the added value of fine temporal resolution time-series products, land surface models at medium spatial resolution can benefit from more precise information on land surface characteristics than simple discrete class designations. This is especially so in spatially heterogeneous environments, where critical information may be lost by classifying complex, intergrading land surfaces as discrete classes which can be converted but not undergo subtle changes in intensity [13], [14]. Continuous fields pixel values offer several advantages over discrete classifications by retaining maximum information content and more precisely characterizing subpixel heterogeneity [15].

Due to the demand for automated workflows for producing temporally dense, continuous fields land surface time series, we developed the automatic adaptive signature generalization and regression (AASGr) algorithm. AASGr builds upon

Manuscript received December 4, 2018; revised March 8, 2019; accepted May 1, 2019. *(Corresponding author: Christopher R. Hakkenberg.)*

C. R. Hakkenberg is with the Department of Statistics, Rice University, Houston, TX 77005 USA, and also with the Kinder Institute for Urban Research, Rice University, Houston, TX 77030 USA (e-mail: ch55@rice.edu; chrishakkenberg@gmail.com).

M. P. Dannenberg is with the Department of Geographical and Sustainability Sciences, The University of Iowa, Iowa City, IA 52242 USA (e-mail: matthew-dannenberg@uiowa.edu).

C. Song is with the Department of Geography, The University of North Carolina at Chapel Hill, Chapel Hill, NC 27599 USA (e-mail: csong@email.unc.edu).

G. Vinci is with the Department of Statistics, Rice University, Houston, TX 77005 USA (e-mail: gv9@rice.edu).

Color versions of one or more of the figures in this letter are available online at http://ieeexplore.ieee.org.

Digital Object Identifier 10.1109/LGRS.2019.2915320

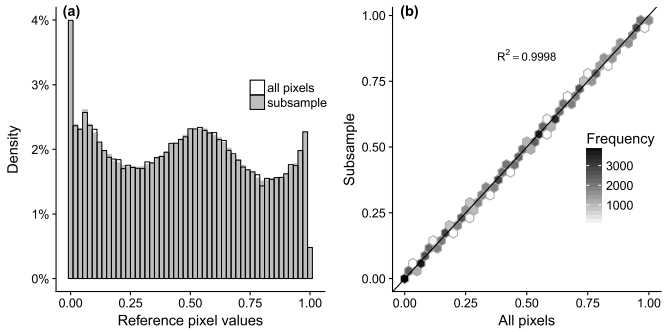

Fig. 1. Reference map subsampling. (a) Density histogram for reference pixel values from NLCD 2001 impervious and subsampled pixels. (b) QQ plot for all reference pixel values versus those in the subsample.

AASG classification—a training data selection algorithm that adapts to image noise and interscene variation [16], [17]—to automate the prediction of continuous fields land surface characteristics based on a single reference map and time-series imagery. AASGr, thus, circumvents the resource-intensive and error-prone process of manual training data selection, while ensuring that all models in the series are individually tuned to unique image characteristics and optimized for predictive accuracy.

This letter consists of four components: A description of the AASGr algorithm (Section II-A), experimental implementation to quantify subannual impervious fractional cover dynamics over a 22-year time series in Houston, TX (Section II-B), a three-part validation of the map time series (Sections II-C and III), and a short discussion of applications and implications for the novel class of products enabled by AASGr (Section IV).

II. Methods

A. AASGr Training Data Selection and Predictive Modeling

Provided a reference image (I_R) paired with a reference map (M_R) from the same date, AASG automates training data selection for prediction in a spatially coincident stack of target imagery (I_T) by first delineating "stable sites"—locations ostensibly not experiencing land cover change between the dates of the I_R and I_T [17]—which are used as the basis for signature extension from the reference date to the target date(s). To do this, a series of image differences (ΔI_i) is created, where

$$\Delta I_i = I_R[x, y, z_i] - I_T[x, y, z_i]; \quad i = 1 \ldots k \tag{1}$$

in the xy coordinate plane for the ith among k spectral bands (z). Under the assumption that the majority of a sufficiently large landscape did not undergo land cover change between the dates of the I_R and I_T, pixels with stable land cover will tend to have ΔI values located at or near the mode of the image difference histogram. By extension, unstable sites-pixels having experienced significant land cover change—possess ΔI values significantly dislocated from the histogram mode. Because modal values are relative to the two images in question, stable sites reflect relative stability between dates rather than absolute spectral differences between images [17]. Thereafter, band-specific difference images are combined into a multiband difference image (ΔI), defined as

$$\Delta I = \sum_{i=1}^{k} |\text{Mode}(\Delta I_i) - \Delta I_i| \tag{2}$$

where a pixel value of 0 in the ΔI would be expected for a maximally stable pixel that exhibits the minimum possible (relative) spectral difference between dates among all k bands.

Concurrently, a spatio-temporally coincident reference map (M_R) consisting of continuous or consecutive integer values of the response variable in question is stratified into m bins $A_1, \ldots, A_m$ spanning the range of pixel values in the M_R. Then, for each $b = 1, \ldots, m$, we select pixels $P_1^b, \ldots, P_{N_b}^b$ according to

$$N_b = \left\lfloor N \times \frac{1}{T} \sum_{h,l} I(M_{R[h,l]} \epsilon A_b) \right\rceil \tag{3}$$

$$D_b = \{(h, l) : M_{R[h,l]} \in A_b, \quad \Delta I_{[h,l]} \leq \bar{\Delta}\} \tag{4}$$

$$P_t^b \mid \left\{P_s^b\right\}_{s<t} \sim \text{Uniform}\left(D_b \setminus \left\{P_s^b\right\}_{s<t}\right) \tag{5}$$

where $\bar{\Delta} = \sigma\Delta I \times c$, $\sigma\Delta I$ is the standard deviation of the values in ΔI, c is a user-defined threshold parameter regulating the maximum allowed total sample size N, T is the total number of pixels in M_R, $\lfloor w \rceil$ denotes the w rounded to the nearest integer, and (h, l) denotes a pixel location. That is, pixels are randomly sampled without replacement from each of the m sets D_b, whose corresponding value in the ΔI is less than a threshold $\bar{\Delta}$ defining the set of stable sites. To ensure a maximally representative training data set optimized for prediction on independent data, the number N_b of stable site pixels sampled from each set D_b is proportional to the number of pixels in the full M_R whose values fall in A_b. For example, for a Landsat image, the distribution of subsampled pixels ($n = 1 \times 10^6$) will closely resemble ($R^2 = 0.99$) that of the full data set ($n = 6 \times 10^{10}$), though at a fraction of the size and consisting of only the most stable site pixels for model training (Fig. 1). Provided that m is large enough to capture the full distribution of values in the M_R, the number of bins for stratification is user-defined.

While *a priori* training data stratification and proportional allotment provide an efficient method for sampling stable site pixels among bins, sampled pixels $P = \{P_t^b\}$ in the M_R retain their original continuous integer values. Once the location of all stable site pixels in the M_R is determined, a full training data set is compiled from the stable site values in the M_R and spatially corresponding pixels in the I_T to predict a continuous fields target map (M_T) and associated uncertainties from the full I_T.

To summarize, the algorithmically generated training data set exhibits three desirable properties.

1) *Multi-Band Stable Sites*: sampled pixels exhibit the minimum relative spectral difference across multiple spectral bands between dates in reference and target imagery.
2) *Proportional Allotment*: the distribution of sample values is proportional to that of the full reference map, thereby ensuring representation across the range of parameter space for optimized prediction on an independent dataset.
3) *Random Stratified Sampling*: within stratified bins of candidate stable sites, sample selection is randomized.

AASGr is not beholden to any one sensor or regression model, and in this experiment, predictive regression was performed on Landsat imagery using random forests (RFs), an ensemble of regression trees based on votes across bootstrap replicates [18]. As an ensemble algorithm with predictors randomly permuted at tree nodes, RF is able to efficiently handle data noise and is noted for its record of high predictive

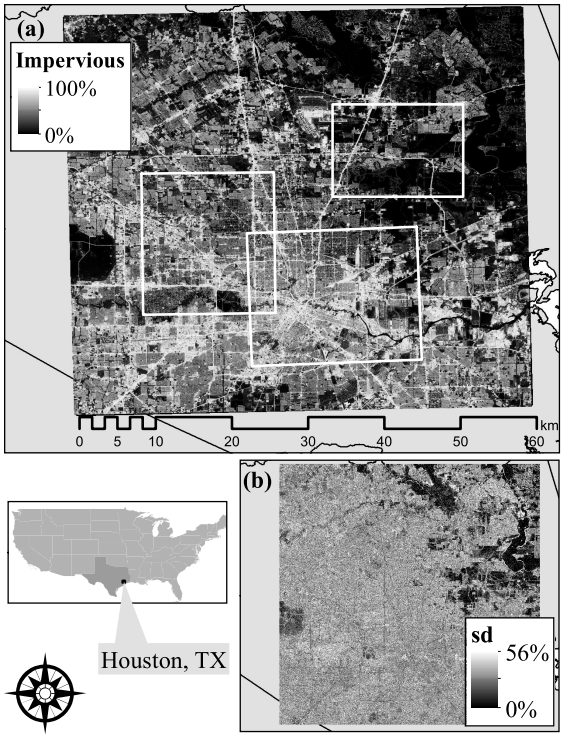

Fig. 2. Houston, TX, study area. (a) Predicted impervious fractional cover for August 28, 2011, where insets refer to the extent of validation images. (b) Standard deviation of the RF's predictive posterior distribution.

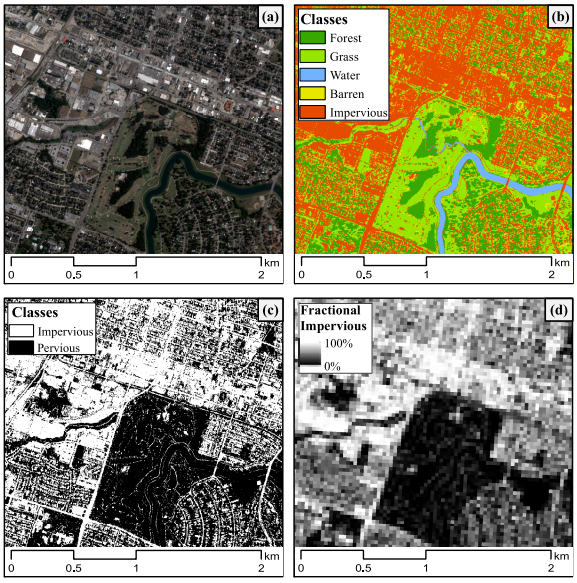

Fig. 3. Validation map (M_V) classification. (a) 3-m resolution validation imagery (I_V). (b) Validation classification (C_V) at 3-m I_V native resolution. (c) 3-m binary pervious/impervious C_V. (d) Resampled impervious cover validation map (M_V) at a 30-m Landsat spatial resolution.

accuracy and generalizability [19]. These properties make it attractive for Landsat image time series, as RF has been shown to effectively handle collinearity among spectral bands, noise due to atmospheric and radiometric contamination, or georegistration issues arising from image misalignment [19].

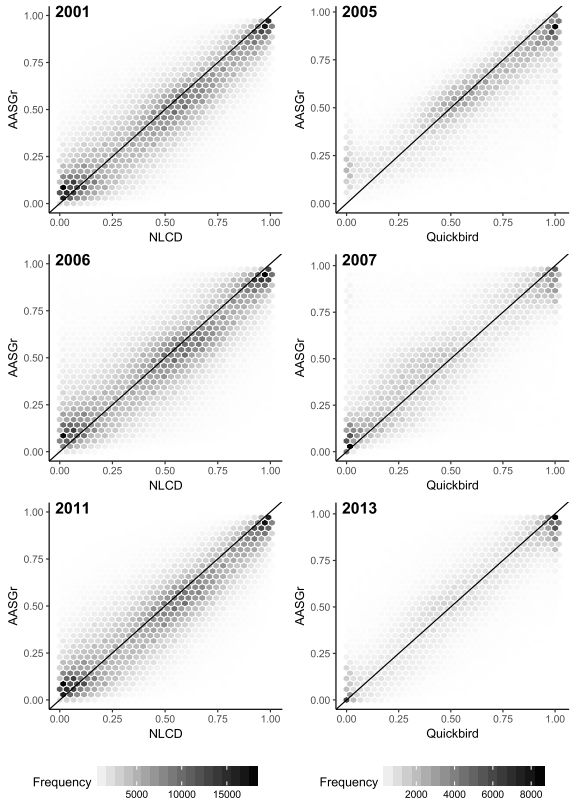

Fig. 4. Validation results. (Left column) AASGr prediction versus NLCD agreement and (Right column) independently classified, 3-m resolution Quickbird images.

TABLE I
AGREEMENT AND VALIDATION

Validation Data	Year	adj-R^2	RMSE	MAE	bias
NLCD	2001	0.82	0.14	0.09	0.01
NLCD	2006	0.77	0.16	0.11	0.02
NLCD	2011	0.77	0.16	0.11	-0.01
Quickbird	2005	0.72	0.15	0.11	-0.05
Quickbird	2007	0.80	0.14	0.11	0.03
Quickbird	2013	0.79	0.14	0.11	-0.01

B. Experimental Implementation

AASGr was tested on a 22-year Landsat image stack covering a 2720 km ^{2} portion of central Houston, TX [see Fig. 2(a)]. Houston's spatially heterogeneous cover and its rapid growth from 1997 to 2018 make it a compelling test case for assessing the performance of AASGr to detect fractional impervious cover as a continuous field. Imagery consisted of all available radiometrically calibrated and orthorectified Landsat Collection 1 Level-1 imagery (WRS2 path/row 25/39) possessing $<10\%$ cloud cover. In total, 66 images fulfilled these criteria. Imagery spanned a range of phenological states (DOYs) and atmospheric conditions, over a range of three satellites/sensors: Landsat-5 TM between 1997 and 2011, Landsat 7 ETM+ for 1999–2012, and Landsat 8 OLI for 2013–2018. Reference maps (M_R) consist of wall-to-wall subpixel impervious fraction maps possessing continuous values between 0.00 and 1.00 from the U.S. Geological Service (USGS) National Land Cover Database (NLCD) Percent Developed Imperviousness product from 2001, 2006, and 2011 [12]. The three reference maps were paired with Landsat reference imagery for each respective year and applied to the most temporally proximate

target imagery (i.e., I_{R-2001} and M_{R-2001} were paired with $I_{T-1997} - I_{T-2003}$, I_{R-2006} and M_{R-2006} with $I_{T-2004} - I_{T-2008}$, and I_{R-2011} and M_{R-2011} with $I_{T-2009} - I_{T-2018}$).

Before prediction, all clouds, cloud shadows, ETM+ SLC-off gaps, and radiometrically saturated or contaminated pixels were algorithmically masked based on quality assessment bands [20]. Except for these masked areas, which are treated as data gaps in all predicative modeling, RF regression models yield posterior predictive distributions based on the votes of all trees in the RF model [21]. Lacunae are interpolated *post hoc*, based on temporally adjacent pixels in the prediction time series. For this interpolation procedure, a low-pass filter using a Gaussian kernel in a five-year window was applied to each pixel in the temporal dimension of the full-time series.

Parameter optimization performed to balance efficiency (run time) and predictive accuracy based on an external comparison with independent NLCD maps resulted in the selection of 140 000 pixels as the total sample size (N) and ten bins (m), with RF hyperparameters: 300 trees per model and 1 predictor sampled at each split. Sensitivity analysis confirmed that model performance was largely robust to parameter values. Among all Landsat band combinations and derived indices, the difference of the blue and near-infrared bands yielded the highest prediction accuracies in model testing and was thereby adopted for all model runs. To prevent the mischaracterization of temporarily docked waterborne vessels as terrestrial impervious surface, a mask based on unchanged water pixels in NLCD 2001 and 2011 maps was applied to the full-time series.

C. Accuracy Assessment

Predictive maps were validated via a three-part accuracy assessment. First, an in-sample out of bag (OOB) estimate of model performance (pseudo-R^2) was derived for every model run. Second, all pixels in predictive maps were compared with NLCD impervious maps for coincident years (i.e., 2001, 2006, and 2011), and the strength of their agreement was assessed via adjusted R^2. To maintain the independence of training and validation data, training data were constrained to the two NLCD-Landsat sets not corresponding to the year of prediction, and their results averaged to produce a single metric of agreement.

As the third test of map accuracy, three 3-m resolution Quickbird validation images (I_V) from 2005, 2007, and 2013 were used for independent validation with spatio-temporally coincident map subsets [Fig. 2(a)]. Cloud masks and regions of interest for five primary land cover types (forest, grassland, urban, water, and barren) in the I_V were manually delineated and used to train an RF classifier. The resulting validation maps possess five-class overall accuracies of 0.83, 0.84, and 0.85 for the three dates, respectively, with the largest confusion occurring between Barren and Urban classes—a not uncommon result in urban classification [22]. Thereafter, the five-class validation classification (C_V) was converted to a binary urban–nonurban classification and resampled to a 30-m resolution validation map (M_V) based on the aggregate of all urban (impervious) subpixels. Aggregated, binary urban–nonurban validation maps possess overall accuracies of 0.91, 0.91, and 0.92, respectively. Subpixel impervious fraction in the resampled M_V is calculated as

$$M_{V[h,l]} = \frac{\sum_{p=1}^{N} C_{Vp}^{[h,l]}}{N} \tag{6}$$

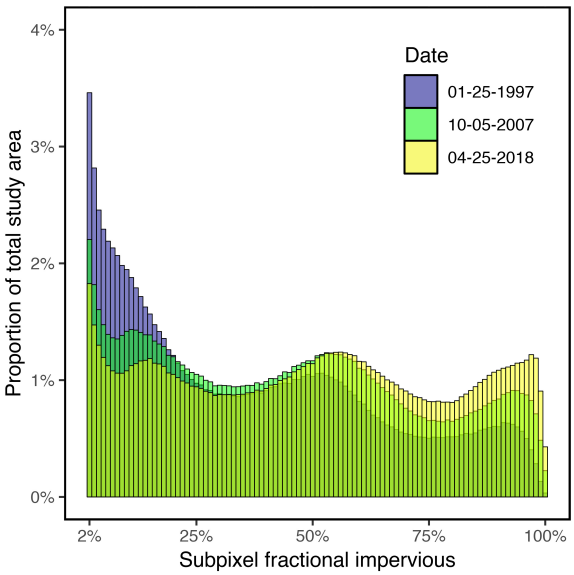

Fig. 5. Continuous change in impervious cover for three dates in Houston, TX. Intermediate colors represent the overlap between dates.

where N is the total number of pixels in C_V corresponding to pixel (h, l) in the M_V. For example, for a 3-m binary C_V, a single 30-m aggregate pixel consists of 100 subpixels, each possessing a value of 0 (pervious) or 1 (impervious). Summing the subpixels and dividing by 100 renders an estimated subpixel impervious fraction in the M_V at the coarser 30-m resolution (Fig. 3). Thus devised, AASGr-generated maps (M_T) can be directly compared with corresponding pixels in the validation subsets in the M_V and assessed for accuracy based on adj-R^2.

III. Results

In experiments, internal OOB pseudo-R^2 for all 66 image predictions ranged from 0.76 to 0.90 ($\mu = 0.83$ and $\sigma = 0.03$) [23]. Visual observation confirms that AASGr-generated maps accurately reproduce known patterns in impervious surface cover [Fig. 2(a)]. The standard deviation of posterior votes serves as a measure of certainty [Fig. 2(b)]. When compared to corresponding, but independent NLCD maps from dates not used for model training, AASGr predictions showed a high degree of agreement based on adj-R^2 (Table I). As no one map is authoritative, the agreement does not directly correspond with accuracy and could reflect or obscure errors in any one image or errors in both [4].

Independent accuracy assessment using three classified and resampled fine-resolution images indicate accuracies in line with NLCD agreement metrics, and comparable to those observed in other studies [13]–[15], though with the added benefit of a continuous fields output at a subannual resolution (Table I). Scatter charts of the agreement show a slight deviation from the 1:1 line, indicative of some boundary bias (Fig. 4; Table I). This compression of the posterior distribution reflects empirical limitations of ensemble classifiers that, while optimizing total accuracy, extract predictions from the mean of the vote posterior and thereby tend to underestimate extreme values at the poles of the range [24].

IV. Discussion

AASGr fully automates model parameterization and prediction of a continuous fields response variable from time-series

imagery, achieving high predictive accuracy in experiments as it efficiently adapts to inconsistencies in multitemporal imagery. Automated signature generalization algorithms are noteworthy as streamlined workflows enable the estimation of land surface characteristics at previously elusive spatio-temporal resolutions. And, unlike discrete classifications, continuous fields regression is optimally suited for producing confidence intervals critical to secondary applications—such as estimating unbiased areal land cover change estimates or as input maps for process-based land surface models—requiring uncertainty estimates of state values [3], [4].

In this implementation, AASGr was tested on a Landsat imagery time series to estimate subannual subpixel impervious fractional cover over a 22-year period in the rapidly urbanizing city of Houston, TX. The resulting map time series is significant in that it showcases the utility of AASGr to quantify subannual land cover dynamics and subpixel heterogeneity (Fig. 5). Therefore, AASGr-enabled time series are capable of simultaneously characterizing both urban extensification (conversion of pervious to impervious surface) and intensification (changing intensity of fractional impervious cover in any one pixel)—a feat otherwise unattainable with hard classifiers. This level of precision is noteworthy for the next-generation urban land cover change applications requiring precise characterizations of land cover change morphologies along a continuum of spatio-temporal change. Land cover time series that is near continuous in space and time offers several advantages to coarse spatial resolution, temporally-sparse time series by more precisely capturing heterogeneity in spatially complex areas, thereby better lending themselves to the derivation of indices of continuous surface metrology [25].

V. Conclusion

In this letter, we present the AASGr algorithm. AASGr is fully automated for time-series prediction in that it is adaptive to the spectral and radiometric characteristics of target imagery and thereby requires neither atmospheric correction nor data normalization. Provided a robust reference map paired with an image from the same date, AASGr can predict highly accurate continuous response values and associated uncertainties for time-series imagery before and after the reference date. This quality makes it attractive for diverse applications requiring multidate land surface information, where reference data are otherwise limited. In this implementation, we tested AASGr for estimating fractional impervious cover in a rapidly urbanizing city, demonstrating its capacity to characterize heterogeneity and intensity in spatially complex areas, as well as higher order temporal dynamics and change rates. AASGr is not limited to estimating subpixel land cover fractions and is amenable to a range of applications requiring dense, continuous fields raster map time series with uncertainty estimates including land surface characteristics like leaf area index, biomass, and albedo.

References

[1] A. S. Belward and J. O. Skøien, "Who launched what, when and why; trends in global land-cover observation capacity from civilian earth observation satellites," *ISPRS J. Photogramm. Remote Sens.*, vol. 103, pp. 115–128, May 2015.

[2] C. R. Hakkenberg, M. P. Dannenberg, C. Song, and K. B. Ensor, "Characterizing multi-decadal, annual land cover change dynamics in Houston, TX based on automated classification of Landsat imagery," *Int. J. Remote Sens.*, vol. 40, no. 2, pp. 693–718, 2019.

[3] A. M. Fox *et al.*, "Evaluation of a data assimilation system for land surface models using CLM4.5," *J. Adv. Model. Earth Syst.*, vol. 10, no. 10, pp. 2471–2494, 2018.

[4] P. Olofsson, G. M. Foody, M. Herold, S. V. Stehman, C. E. Woodcock, and M. A. Wulder, "Good practices for estimating area and assessing accuracy of land change," *Remote Sens. Environ.*, vol. 148, pp. 42–57, May 2014.

[5] Z. Zhu, "Change detection using Landsat time series: A review of frequencies, preprocessing, algorithms, and applications," *ISPRS J. Photogramm. Remote Sens.*, vol. 130, pp. 370–384, Aug. 2017.

[6] B. L. Markham and D. L. Helder, "Forty-year calibrated record of earth-reflected radiance from Landsat: A review," *Remote Sens. Environ.*, vol. 122, pp. 30–40, Jul. 2012.

[7] J. E. Vogelmann, A. L. Gallant, H. Shi, and Z. Zhu, "Perspectives on monitoring gradual change across the continuity of Landsat sensors using time-series data," *Remote Sens. Environ.*, vol. 185, pp. 258–270, Nov. 2016.

[8] C. Song, C. E. Woodcock, K. C. Seto, M. P. Lenney, and S. A. Macomber, "Classification and change detection using Landsat TM data: When and how to correct atmospheric effects?" *Remote Sens. Environ.*, vol. 75, no. 2, pp. 230–244, 2001.

[9] C. Gómez, J. C. White, and M. A. Wulder, "Optical remotely sensed time series data for land cover classification: A review," *ISPRS J. Photogramm. Remote Sens.*, vol. 116, pp. 55–72, Jun. 2016.

[10] Z. Zhu, C. E. Woodcock, C. Holden, and Z. Yang, "Generating synthetic Landsat images based on all available Landsat data: Predicting Landsat surface reflectance at any given time," *Remote Sens. Environ.*, vol. 162, pp. 67–83, Jun. 2015.

[11] G. Yin, G. Mariethoz, Y. Sun, and M. F. McCabe, "A comparison of gap-filling approaches for Landsat-7 satellite data," *Int. J. Remote Sens.*, vol. 38, no. 23, pp. 6653–6679, 2017.

[12] G. Z. Xian, C. G. Homer, J. Dewitz, J. Fry, N. Hossain, and J. Wickham, "Change of impervious surface area between 2001 and 2006 in the conterminous United States," *Photogramm. Eng. Remote Sens.*, vol. 77, no. 8, pp. 758–762, 2011.

[13] C. Deng and Z. Zhu, "Continuous subpixel monitoring of urban impervious surface using Landsat time series," *Remote Sens. Environ.*, to be published.

[14] D. Lu and Q. Weng, "Use of impervious surface in urban land-use classification," *Remote Sens. Environ.*, vol. 102, nos. 1–2, pp. 146–160, 2006.

[15] P. Wang, C. Huang, and E. C. B. de Colstoun, "Mapping 2000–2010 impervious surface change in india using global land survey Landsat data," *Remote Sens.*, vol. 9, no. 4, p. 366, 2017.

[16] M. P. Dannenberg, C. R. Hakkenberg, and C. Song, "Consistent classification of Landsat time series with an improved automatic adaptive signature generalization algorithm," *Remote Sens.*, vol. 8, no. 8, p. 691, 2016.

[17] J. Gray and C. Song, "Consistent classification of image time series with automatic adaptive signature generalization," *Remote Sens. Environ.*, vol. 134, pp. 333–341, Jul. 2013.

[18] L. Breiman, "Random forests," *Mach. Learn.*, vol. 45, no. 1, pp. 5–32, Oct. 2001.

[19] P. O. Gislason, J. A. Benediktsson, and J. R. Sveinsson, "Random Forests for land cover classification," *Pattern Recognit. Lett.*, vol. 27, no. 4, pp. 294–300, Mar. 2006.

[20] Z. Zhu, S. Wang, and C. E. Woodcock, "Improvement and expansion of the Fmask algorithm: Cloud, cloud shadow, and snow detection for Landsats 4–7, 8, and Sentinel 2 images," *Remote Sens. Environ.*, vol. 159, pp. 269–277, Mar. 2015.

[21] A. Liaw and M. Wiener, "Classification and regression by randomForest," *R News*, vol. 2, no. 3, pp. 18–22, 2002.

[22] P. S. Kaspersen, R. Fensholt, and M. Drews, "Using Landsat vegetation indices to estimate impervious surface fractions for European cities," *Remote Sens.*, vol. 7, no. 6, pp. 8224–8249, 2015.

[23] C. R. Hakkenberg, "Houston Subannual Percent Impervious (SPI) land cover dataset: 1997–2018," in *Kinder Institute Urban Data Platform*. Houston, TX, USA: Kinder Institute, 2019. doi: 10.25612/837.d8nxbzwj01ad.

[24] E. Grossmann, J. Ohmann, J. Kagan, H. May, and M. Gregory, "Mapping ecological systems with a random forest model: Tradeoffs between errors and bias," *Gap Anal. Bull.*, vol. 17, pp. 16–22, Feb. 2010.

[25] K. McGarigal, S. Tagil, and S. A. Cushman, "Surface metrics: An alternative to patch metrics for the quantification of landscape structure," *Landscape Ecology*, vol. 24, no. 3, pp. 433–450, 2009.